Super-Resolution via Spatial Mode Demultiplexing and its Applicability to Observational Astronomy

Final Report

Authors: J. Řeháček[1], Z. Hradil[1], B. Stoklasa[1], M. Paúr[1], L. Moťka[1], L.L. Sánchez-Soto[2,3], J. Grover[4], A. Kržič[4]

Affiliation: [1]Palacky University Olomouc, [2]Universidad Complutense Madrid, [3]Max-Planck-Institut fur die Physik des Lichts, Erlangen, [4]ESA ACT

Date: December 20, 2017

Contacts:

Jaroslav Řeháček, Dept. of Optics, Palacky University, 17. listopadu 12, 77146 Olomouc, Czech Republic
Tel: +420585634257
Fax:
e-mail: rehacek@optics.upol.cz

Leopold Summerer (Technical Officer)
Tel: +31(0)715654192
Fax: +31(0)715658018
e-mail: act@esa.int

Available on the ACT website
http://www.esa.int/act

Ariadna ID: 17/1501
Ariadna study type: Standard
Contract Number: 4000120780/17/NL/LF/as

I. OBJECTIVES

Super-resolution in optical imaging means enhancing the resolution of the system beyond what is considered to be the classical limit of conventional imaging systems. In June 2017, an ARIADNA collaboration between researchers of Palacky University (Czech Republic) and the European Space Agency's Advanced Concepts Team (ACT) started on super-resolution for astronomical applications, with the following ambitious objectives:

1. Setting an appropriate model for two unequally bright incoherent point sources
2. Calculating the quantum Fisher information matrix and the related quantum bounds on precision for simultaneous estimation of geometrical centroid, separation and relative brightness of the two sources
3. Finding an optimal measurement scheme that would saturate the quantum bounds from 2.
4. Experimentally verifying 3.

The project has achieved significant progress on the first three objectives, leading to two dedicated publications, with the results detailed in this report. With regard to the experimental implementation, it became apparent over the course of the project that the approach of spatial mode demultiplexing using amplitude modulation together with a cross-correlation principle, while suitable as a proof of concept, is very inefficient; this is because only a small fraction of the incoming photons contribute to the detected signal.

As such a more efficient, and practically more feasible, approach based on phase modulation was identified. Preliminary simulations have indicated that a setup outperforming conventional imaging in practice can be realized using a (combination of) phase mask(s). Pursuing this promsing research line will be an objective of future work. While working on spatial super-resolution of point sources, we also realized that similar principles can be applied to achieve *spectral* super-resolution, which is particularly interesting since spectroscopy is equally or maybe even more important for astronomical applications. This too has been identified as a target of future research.

II. INTRODUCTION

The time-honored Rayleigh criterion [1] specifies the minimum separation between two incoherent optical sources using a linear imaging system. As a matter of fact, it is the size of the point spread function [2] that determines the resolution: two points closer than the PSF width will be difficult to resolve due to the substantial overlap of their images.

Until recently, this Rayleigh criterion has been considered as a fundamental limit. Resolution can only be improved either by reducing the wavelength or by building higher numerical-aperture optics, thereby making the PSF narrower. Nonetheless, outstanding methods have been developed lately that can break the Rayleigh limit under special circumstances [3–12]. Though promising, these techniques are involved and require careful control of the source, which is not always possible, especially in astronomical applications.

Despite being very intuitive, the common derivation of the Rayleigh limit is heuristic and it is deeply rooted in classical optical technology [13]. Recently, inspired by ideas of quantum information, Tsang and coworkers [14–17] have revisited this problem using the Fisher information and the associated Cramér-Rao lower bound (CRLB) to quantify how well the separation between two point sources can be estimated. When only the intensity at the image is measured (the basis of all the conventional techniques), the Fisher information falls to zero as the separation between the sources decreases and the CRLB diverges accordingly; this is known as the Rayleigh curse [14]. However, when the Fisher information of the complete field is calculated, it stays constant and so does the CRLB, revealing that the Rayleigh limit is not essential to the problem.

These remarkable predictions prompted a series of experimental implementations [18–21] and further generalizations [22–28], including the related question of source localization [29–31]. All this previous work has focused on the estimation of the separation, taking for granted a highly symmetric configuration with equally bright sources. Here, we approach the issue in a more realistic scenario, where the sources may have unequal intensities. This involves the simultaneous estimation of separation, centroid, and intensities. Typically, when estimating multiple parameters, there is a trade-off in how well different parameters may be estimated: when the estimation protocol is optimized from the point of view of one parameter, the precision with which the remaining ones can be estimated deteriorates.

Actually, we show that including intensity in the estimation problem does lead to a reduction in the information for unbalanced sources. However, the information available in an optimal measurement still surpasses that of a conventional direct imaging scheme by a significant margin at small separations. This suggests possible applications, for example, in observational astronomy, where sources typically have small angular separations and can have large differences in brightness.

III. FORMULATION OF THE ESTIMATION PROBLEM

Let us first set the stage for our simple model. We assume quasimonochromatic paraxial waves with one specified polarization and one spatial dimension, x denoting the image-plane coordinate. The corresponding object-plane coordinates can be obtained via the lateral magnification of the system, which we take to be linear spatially invariant. We emphasize that these assumptions are standard in imaging sciences [2] and they do not alter our main conclusions.

To facilitate possible generalizations, we phrase what follows in a quantum parlance. A wave of complex amplitude $U(x)$ can thus be assigned to a ket $|U\rangle$, such that $U(x) = \langle x|U\rangle$, where $|x\rangle$ is a vector describing a point-like source at x.

The system is characterized by its PSF, which represents its

normalized intensity response to a point source. We denote this PSF by $I(x) = |\langle x|\Psi\rangle|^2 = |\Psi(x)|^2$, so that $\Psi(x)$ can be interpreted as the amplitude PSF.

Two mutually incoherent point sources, of different intensities and separated by a distance $\mathfrak{s}$, are imaged by that system. The signal can be represented as a density operator

$$\rho_{\boldsymbol{\theta}} = \mathfrak{q}\,\rho_+ + (1-\mathfrak{q})\,\rho_-\,, \tag{1}$$

where $\mathfrak{q}$ and $1-\mathfrak{q}$ are the intensities of the sources, with the proviso that the total intensity is normalized to unity. In addition, we have defined $\rho_\pm = |\Psi_\pm\rangle\langle\Psi_\pm|$ and the x-displaced PSF states are

$$\langle x|\Psi_\pm\rangle = \langle x - \mathfrak{s}_0 \mp \mathfrak{s}/2|\Psi\rangle = \Psi(x - \mathfrak{s}_0 \mp \mathfrak{s}/2), \tag{2}$$

so that they are symmetrically located around the geometric centroid $\mathfrak{s}_0 = \frac{1}{2}(x_+ + x_-)$. Note that

$$|\Psi_\pm\rangle = \exp[-i(\mathfrak{s}_0 \pm \mathfrak{s}/2)P]|\Psi\rangle\,, \tag{3}$$

where P is the momentum operator, which generates displacements in the x variable. As in quantum mechanics, it acts as a derivative $P = -i\partial_x$. These spatial modes are not orthogonal ($\langle\Psi_-|\Psi_+\rangle \neq 0$), so they cannot be separated by independent measurements.

We stress that, by its very nature, a point-like source is specified by a Dirac delta complex amplitude, which results in a spatially coherent optical field. This justifies treating the spatial degrees of freedom of both signal components as pure states [32].

The density matrix $\rho_{\boldsymbol{\theta}}$ gives the normalized mean intensity

$$\rho_{\boldsymbol{\theta}}(x) = \mathfrak{q}\,|\Psi(x - \mathfrak{s}_0 - \mathfrak{s}/2)|^2 + (1-\mathfrak{q})\,|\Psi(x - \mathfrak{s}_0 + \mathfrak{s}/2)|^2\,, \tag{4}$$

and depends on the centroid $\mathfrak{s}_0$, the separation $\mathfrak{s}$, and the relative intensities of the sources $\mathfrak{q}$. This is indicated by the vector $\boldsymbol{\theta} = (\mathfrak{s}_0, \mathfrak{s}, \mathfrak{q})^t$.

IV. MULTIPARAMETER CRAMÉR-RAO LOWER BOUNDS

The task is to estimate the values of $\boldsymbol{\theta}$ through the measurement of some observables on $\rho_{\boldsymbol{\theta}}$. In turn, a quantum estimator $\widehat{\boldsymbol{\theta}}$ for $\boldsymbol{\theta}$ is a selfadjoint operator representing a proper measurement followed by data processing performed on the outcomes. Such a parameter estimation implies uncertainties for the measured values, which cannot be avoided.

In this multiparameter estimation scenario, the central quantity is the quantum Fisher information matrix (QFIM) [33]. This is a natural generalization of the classical Fisher information, which is a mathematical measure of the sensitivity of an observable quantity to changes in its underlying parameters. However, the QFIM is optimized over all the possible quantum measurements. It is defined as

$$\mathcal{Q}_{\alpha\beta}(\boldsymbol{\theta}) = \tfrac{1}{2}\,\mathrm{Tr}(\rho_{\boldsymbol{\theta}}\{L_\alpha, L_\beta\})\,, \tag{5}$$

where the Greek indices run over the components of the vector $\boldsymbol{\theta}$ and $\{\cdot,\cdot\}$ denotes the anticommutator. Here, L_α stands for the symmetric logarithmic derivative [34] with respect the parameter θ_α, represented implicitly as

$$\tfrac{1}{2}(L_\alpha\rho_{\boldsymbol{\theta}} + \rho_{\boldsymbol{\theta}}L_\alpha) = \partial_\alpha\rho_{\boldsymbol{\theta}}\,, \tag{6}$$

with $\partial_\alpha = \partial/\partial\theta_\alpha$.

Upon writing $\rho_{\boldsymbol{\theta}}$ in its eigenbasis, $\rho_{\boldsymbol{\theta}} = \sum_n \lambda_n|\lambda_n\rangle\langle\lambda_n|$, the QFIM can be concisely expressed as [35]

$$\mathcal{Q}_{\alpha\beta}(\boldsymbol{\theta}) = 2\sum_{m,n}\frac{1}{\lambda_m + \lambda_n}\langle\lambda_m|\partial_\alpha\rho_{\boldsymbol{\theta}}|\lambda_n\rangle\langle\lambda_n|\partial_\beta\rho_{\boldsymbol{\theta}}|\lambda_m\rangle\,, \tag{7}$$

and the summation extends over m,n with $\lambda_m + \lambda_n \neq 0$.

The QFIM is a distinguishability metric on the space of quantum states and leads to the multiparameter quantum CRLB [36, 37] for a single detection event:

$$\mathrm{Cov}(\widehat{\boldsymbol{\theta}}) \geq \mathcal{Q}^{-1}(\boldsymbol{\theta})\,, \tag{8}$$

where $\mathrm{Cov}_{\alpha\beta}(\widehat{\boldsymbol{\theta}}) = \mathbb{E}[(\widehat{\theta}_\alpha - \theta_\alpha)(\widehat{\theta}_\beta - \theta_\beta)]$ refers to the covariance matrix for a locally unbiased estimator $\widehat{\boldsymbol{\theta}}$ of the quantity $\boldsymbol{\theta}$ and $\mathbb{E}[Y]$ is the expectation value of the random variable Y. The above inequality should be understood as a matrix inequality. In general, we can write $\mathrm{Tr}[G\mathrm{Cov}(\widehat{\boldsymbol{\theta}})] \geq \mathrm{Tr}[G\mathcal{Q}^{-1}(\boldsymbol{\theta})]$, where G is some positive cost matrix, which allows us to asymmetrically prioritise the uncertainty cost of different parameters.

In using Eq. (8) we implicitly assume that the measurement is repeated N times, and this number is large. In astronomy, this corresponds to collecting many photons from the measured source, which is always the case, even for the stars at the detection limit of the telescope. For N detections, the right hand side of Eq. (8) is divided by N. Thanks to this simple proportionality, factor N can be omitted and always reintroduced into the final expressions if needed.

The individual parameter θ_α can be estimated with a variance satisfying $\mathrm{Var}(\widehat{\theta}_\alpha) \geq (\mathcal{Q}^{-1})_{\alpha\alpha}(\boldsymbol{\theta})$, and a positive operator-valued measurement (POVM) attaining this accuracy is given by the eigenvectors of L_α. Unlike for a single parameter, the collective bound is not always saturable: the intuitive reason for this is incompatibility of the optimal measurements for different parameters [38].

If the operators L_α corresponding to the different parameters commute, there is no additional difficulty in extracting maximal information from a state on all parameters simultaneously. If they do not commute, however, this does not immediately imply that it is impossible to simultaneously extract information on all parameters with precision matching that of the separate scenario for each. As discussed in a number of papers [39–41] the multiparameter quantum CRLB can be saturated provided

$$\mathrm{Tr}(\rho_{\boldsymbol{\theta}}[L_\alpha, L_\beta]) = 0\,, \tag{9}$$

with $[\cdot,\cdot]$ being the commutator. Then, optimal measurements can be found by optimizing over the classical Fisher information, as the QFIM is an upper bound for the former quantity. This can be efficiently accomplished by global optimization algorithms. For our particular case, it is easy

to see that the condition (9) is fulfilled whenever the PSF is real, $\Psi(x)^* = \Psi(x)$, which will be assumed henceforth. Additionally, for $N \gg 1$ the classical CRLB of the optimal measurement (i.e., the quantum CRLB) can be saturated with maximum-likelihood estimators. In the following we may thus replace all inequalities with their corresponding upper/lower bounds.

To proceed further, we note that the density matrix $\rho_{\boldsymbol{\theta}}$ is, by definition, of rank 2. The QFIM reduces then to the simpler form

$$\begin{aligned} Q_{\alpha\beta} = &-\frac{3}{\lambda_1}\langle\lambda_1|\partial_\alpha\rho_{\boldsymbol{\theta}}|\lambda_1\rangle\langle\lambda_1|\partial_\beta\rho_{\boldsymbol{\theta}}|\lambda_1\rangle \\ &-\frac{3}{\lambda_2}\langle\lambda_2|\partial_\alpha\rho_{\boldsymbol{\theta}}|\lambda_2\rangle\langle\lambda_2|\partial_\beta\rho_{\boldsymbol{\theta}}|\lambda_2\rangle \\ &+4\left(1-\frac{1}{\lambda_1}-\frac{1}{\lambda_2}\right)\langle\lambda_1|\partial_\alpha\rho_{\boldsymbol{\theta}}|\lambda_2\rangle\langle\lambda_2|\partial_\beta\rho_{\boldsymbol{\theta}}|\lambda_1\rangle \\ &+\frac{4}{\lambda_1}\langle\lambda_1|\partial_\alpha\rho_{\boldsymbol{\theta}}\partial_\beta\rho_{\boldsymbol{\theta}}|\lambda_1\rangle+\frac{4}{\lambda_2}\langle\lambda_2|\partial_\alpha\rho_{\boldsymbol{\theta}}\partial_\beta\rho_{\boldsymbol{\theta}}|\lambda_2\rangle \end{aligned} \tag{10}$$

The derivatives involved in this equation can be easily evaluated; the result reads

$$\begin{aligned} \partial_{\mathfrak{s}_0}\rho_{\boldsymbol{\theta}} &= i[\rho_{\boldsymbol{\theta}},P]\,, \\ \partial_{\mathfrak{s}}\rho_{\boldsymbol{\theta}} &= \tfrac{i}{2}(\mathfrak{q}[\rho_+,P]-(1-\mathfrak{q})[\rho_-,P])\,, \\ \partial_{\mathfrak{q}}\rho_{\boldsymbol{\theta}} &= \rho_+-\rho_-\,. \end{aligned} \tag{11}$$

To complete the calculation it proves convenient to write the two nontrivial eigenstates of $\rho_{\boldsymbol{\theta}}$ in terms of non-orthogonal component states $|\Psi_\pm\rangle$: $|\lambda_{1,2}\rangle = a_{1,2}|\Psi_+\rangle + b_{1,2}|\Psi_-\rangle$, where $a_{1,2}$ and $b_{1,2}$ are easy-to-find yet complicated functions of the separation and the intensities and whose explicit form is of no relevance for our purposes here. Substituting this and Eq. (11) into Eq. (10), and after a lengthy calculation, we obtain a compact expression for the QFIM

$$Q = 4\begin{pmatrix} p^2+4\mathfrak{q}(1-\mathfrak{q})\wp^2 & (\mathfrak{q}-1/2)p^2 & -iw\wp \\ (\mathfrak{q}-1/2)p^2 & p^2/4 & 0 \\ -iw\wp & 0 & \dfrac{1-w^2}{4\mathfrak{q}(1-\mathfrak{q})} \end{pmatrix}. \tag{12}$$

This is our central result. The QFIM depends only on the following quantities

$$\begin{aligned} w &\equiv \langle\Psi_\pm|\Psi_\mp\rangle = \langle\Psi|\exp(i\mathfrak{s}P)|\Psi\rangle\,, \\ p^2 &\equiv \langle\Psi_\pm|P^2|\Psi_\pm\rangle = \langle\Psi|P^2|\Psi\rangle\,, \\ \wp &\equiv \pm\langle\Psi_\pm|P|\Psi_\mp\rangle = \langle\Psi|\exp(i\mathfrak{s}P)P|\Psi\rangle\,. \end{aligned} \tag{13}$$

Notice carefully that p^2 is solely determined by the shape of the PSF, whereas both w and $\wp$ (which is purely imaginary) depend on the separation $\mathfrak{s}$.

V. PRECISIONS FOR THE PARAMETER ESTIMATIONS

In what follows, rather than the variances themselves, we will use the inverses

$$H_\alpha = \frac{1}{\mathrm{Var}(\theta_\alpha)}\,, \tag{14}$$

usually called the precisions [42]. In this way, we avoid potential divergences as $\mathfrak{s}\to 0$.

The QFIM (12) nicely shows the interplay between various signal parameters. First, notice that Q is independent of the centroid, as might be expected. Second, for equally bright sources, $\mathfrak{q}=1/2$, the measurement of separation $\mathfrak{s}$ is uncorrelated with the measurements of the remaining parameters and we have $H_{\mathfrak{s}}(\mathfrak{q}=1/2)=p^2$, a well known result, and the Rayleigh curse is lifted [18]. This happy situation does not hold for unequal intensities $\mathfrak{q}\neq 1/2$; now, the separation is correlated with the centroid (via the intensity term $\mathfrak{q}-1/2$) and the centroid is correlated with the intensity (via p^2). This can be intuitively understood: unequal intensities result in asymmetrical images and finding the centroid is no longer a trivial task. This asymmetry, in turn, depends on the relative brightness of the two components. Hence, all the three parameters become correlated and, as we shall see, having separation-independent information about $\mathfrak{s}$ is no longer possible.

Indeed, by inverting the QFIM we immediately get

$$\begin{aligned} H_{\mathfrak{s}_0} &= 4\mathscr{Q}^2\frac{\wp^2+p^2(1-w^2)}{1-w^2}\,, \\ H_{\mathfrak{s}} &= p^2\mathscr{Q}^2\frac{\wp^2+p^2(1-w^2)}{\mathscr{Q}^2\wp^2+p^2(1-w^2)}\,, \\ H_{\mathfrak{q}} &= \frac{4}{\mathscr{Q}^2}\frac{\wp^2+p^2(1-w^2)}{\wp^2+p^2}\,, \end{aligned} \tag{15}$$

where $0<\mathscr{Q}^2\equiv 4\mathfrak{q}(1-\mathfrak{q})\leq 1$. Obviously, $H_{\mathfrak{s}}(\mathfrak{q})\leq H_{\mathfrak{s}}(\mathfrak{q}=1/2)=p^2$ and $\lim_{\mathfrak{q}\to 0,1} H_{\mathfrak{s}}(\mathfrak{q})=0$, which demonstrates that resolving two highly unequal sources is difficult, even at the quantum limit.

The instance of large brightness differences and small separations is probably the most interesting regime encountered, e. g., in exoplanet observations. We first expand the $\mathfrak{s}$-dependent quantities:

$$\begin{aligned} w(\mathfrak{s}) &= \langle\Psi|e^{i\mathfrak{s}P}|\Psi\rangle \simeq 1-\tfrac{1}{2}p^2\mathfrak{s}^2+\tfrac{1}{24}p^4\mathfrak{s}^4, \\ p(\mathfrak{s}) &= \langle\Psi|Pe^{i\mathfrak{s}P}|\Psi\rangle \simeq ip^2\mathfrak{s}-i\tfrac{1}{6}p^4\mathfrak{s}^3\,, \end{aligned} \tag{16}$$

where $p^4=\langle\Psi|P^4|\Psi\rangle$ is the fourth moment of the PSF momentum. Then, as $\mathfrak{s}\ll 1$, we get (for $0<\mathscr{Q}<1$)

$$\begin{aligned} H_{\mathfrak{s}_0} &\simeq \mathscr{Q}^2\,\mathrm{Var}(\hat{P}^2)\,\mathfrak{s}^2\,, \\ H_{\mathfrak{s}} &\simeq \frac{\mathscr{Q}^2}{4(1-\mathscr{Q}^2)}\,\mathrm{Var}(\hat{P}^2)\,\mathfrak{s}^2, \\ H_{\mathfrak{q}} &\simeq \frac{1}{\mathscr{Q}^2}\,\mathrm{Var}(\hat{P}^2)\,\mathfrak{s}^4\,. \end{aligned} \tag{17}$$

The PSF enters these expressions through the variance of P^2: $\mathrm{Var}(\hat{P}^2)=\mathbb{E}[(P^2-p^2)^2]$. This leaves room for optimization, provided the PSF can be controlled. For a fixed PSF, the information about all three parameters vanish with $\mathfrak{s}\to 0$, unless $\mathfrak{q}=1/2$. Since exactly balanced sources are uncommon, the information about very small separations always drops to near

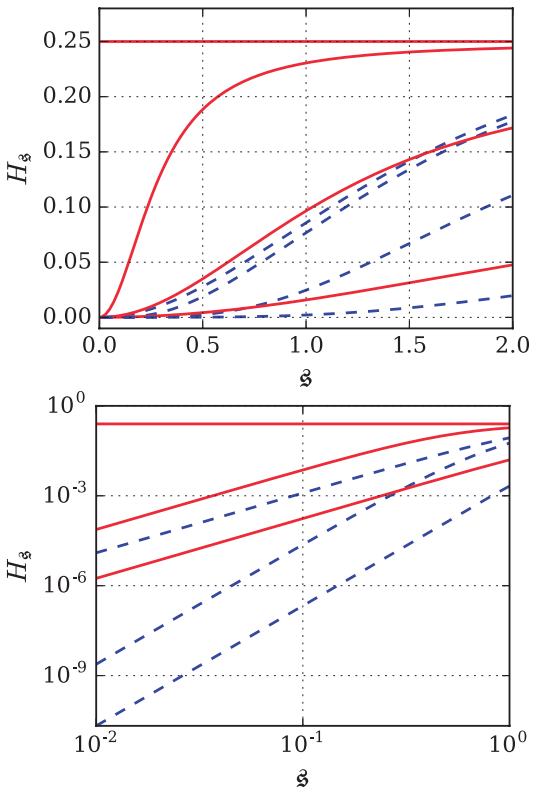

FIG. 1. Upper panel: Precision $H_{\mathfrak{s}}$ in the separation $\mathfrak{s}$ as inferred by optimal (red solid lines) and direct (blue broken lines) detections, for different relative intensities of the two sources. The values of $\mathfrak{q}$, from top to bottom, are 0.5, 0.45, 0.3, and 0.1. Notice that the performance of the optimal detection is rather sensitive to small deviations from equal brightness over a wide range of separations. Lower panel: Precisions visualized on a logarithmic scale. Slopes of straight lines translate to the powers of $\mathfrak{s}$. The values of $\mathfrak{q}$ are, from top to bottom, 0.5, 0.4, and 0.1.

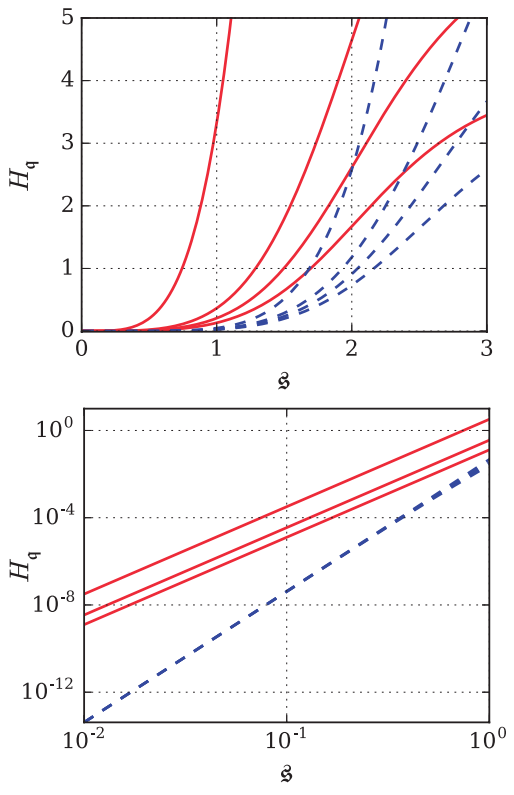

FIG. 2. Upper panel: Precision $H_{\mathfrak{q}}$ in the relative intensity $\mathfrak{q}$ as inferred by optimal (red solid lines) direct (blue broken lines) detections, for different relative intensities of the two sources. The values of $\mathfrak{q}$, from bottom to top are 0.5, 0.2, 0.1, and 0.01. Lower panel: Precisions visualized on a logarithmic scale. Slopes of straight lines translate to the powers of $\mathfrak{s}$. The three blue broken lines cannot be distinguished on this scale. The values of $\mathfrak{q}$ are, from bottom to top, 0.5, 0.2, and 0.01.

zero and the Rayleigh curse is unavoidable. However, significant improvements of the optimal measurement schemes over the standard intensity detection are still possible.

To illustrate this point let us consider a Gaussian response $\langle x|\Psi\rangle = (2\pi)^{1/4}\exp(-x^2/4)$ of unit width, which will serve from now on as our basic unit length. We compare the quantum limit given by (12) with that given by the classical Fisher information for the direct intensity measurement. We assume no prior knowledge about any of the three parameters.

Figure 1 plots information about separation $H_{\mathfrak{s}}$ for different relative intensities $\mathfrak{q}$. Unbalanced intensities make both optimal and intensity detection go to zero for small separations, however the former at a much slower rate. Hence, the ratio of optimal to intensity information increases with decreasing separations, regardless of whether the sources are balanced.

The reason becomes obvious with the same data visualized on the logarithmic scales, as shown in the lower panel of Fig. 1. In the region of $\mathfrak{s} \ll \sigma$, we can discern two regimes of importance. For balanced sources, $H_{\mathfrak{s}}^{\rm opt} \propto 1$ and $H_{\mathfrak{s}}^{\rm int} \propto \mathfrak{s}^2$. For unbalanced sources, $H_{\mathfrak{s}}^{\rm opt} \propto \mathfrak{s}^2$, as we have seen, and $H_{\mathfrak{s}}^{\rm int} \propto \mathfrak{s}^4$. In consequence, there is always a factor of $\mathfrak{s}^{-2}$ improvement of the optimal detection over the standard one, irrespective of the true values of the signal parameters. In practice, this means that when we already are well below the Rayleigh limit, if we decrease the separation 10 times, about 10000 times more photons must be detected with a CCD camera to keep the accuracy of the measurement, while only 100 times more would suffice for optimal measurement. This amounts to saving 99% of detection time with the optimal detection scheme.

Figure 2 presents a similar comparison, but now concerning the precission $H_{\mathfrak{q}}$ in the relative intensity. Here, optimal information and intensity information always scale as $\mathfrak{s}^4$ and $\mathfrak{s}^6$, respectively, and the same $\mathfrak{s}^{-2}$ gain in performance appears. Notice the reversed ordering of curves with $\mathfrak{q}$, meaning that now, the information increases with increasing intensity difference, which reveals the complementarity between these magnitudes. Also notice that the broken lines converge as we approach $\mathfrak{s} = 0$. It can be shown that the leading term for intensity detection for small separations is $\mathfrak{q}$-independent, in contrast to the optimal detection, which displays a strong $H_{\mathfrak{q}}^{\rm opt} \propto \mathfrak{q}^{-1}$ dependence for $\mathfrak{q} \ll 1/2$. This highlights the ad-

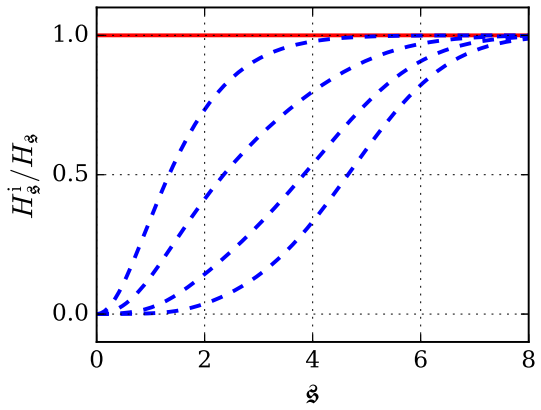

FIG. 3. Precision about separation provided by the direct intensity imaging normalized by the corresponding quantum limit. Notice how the gap between the optimal detection (red solid line) and direct imaging (blue broken lines) widens with the two sources getting more unequal. The values of $\mathfrak{q}$ are, from bottom to top, 0.001, 0.01, 0.1, and 0.5.

vantage of an optimal detection scheme for astronomical observations. For example, more than a quarter of catalogued binary systems consist of stars that differ in brightness by more than an order of magnitude [43], and the darkest known exoplanet is three orders of magnitude dimmer than its host star in the infrared [44].

Finally, Fig. 3 shows that for highly unbalanced sources, the advantage of the quantum detection over the direct intensity imaging extends to larger separations. For balanced sources, ($\mathfrak{q} = 0.5$) direct imaging drops below 50% of the corresponding quantum limit at $\mathfrak{s} \simeq 1.3\sigma$. Tthis border value grows to $\mathfrak{s} \simeq 2.3\sigma$ at $\mathfrak{q} = 0.1$ and further to $\mathfrak{s} \simeq 3.8\sigma$ at $\mathfrak{q} = 0.01$. This means one can benefit from quantum detection well above the Rayleigh limit provided the two signal components are highly unequal, which is often the case.

VI. OPTIMAL MEASUREMENTS FOR QUANTUM SPATIAL SUPER-RESOLUTION

The measured density matrix depends on the centroid $\mathfrak{s}_0$, the separation $\mathfrak{s}$, and the relative intensities of the sources $\mathfrak{q}$. This is indicated by the vector $\boldsymbol{\theta} = (\mathfrak{s}_0, \mathfrak{s}, \mathfrak{q})^t$. Our task is to estimate the values of $\boldsymbol{\theta}$ through the measurement of some observables on $\rho_{\boldsymbol{\theta}}$. In multiparameter estimation, the quantum Cramér-Rao lower bound (CRLB) per single detection event is given by the inequality (8) and Greek indices run the values $\{\mathfrak{s}_0, \mathfrak{s}, \mathfrak{q}\}$.

The individual parameter θ_α can be estimated with a variance satisfying $\mathrm{Var}(\widehat{\theta}_\alpha) \geq (Q^{-1})_{\alpha\alpha}(\boldsymbol{\theta})$. It is convenient to use the inverses of the variances $H_\alpha = 1/\mathrm{Var}(\theta_\alpha)$, usually called the precisions [42]. In the limit of $\mathfrak{s} \to 0$, they turn out to be

$$
\begin{aligned}
H^Q_{\mathfrak{s}_0} &\simeq \mathscr{Q}^2 G_{22}\, \mathfrak{s}^2 + O(\mathfrak{s}^4)\,, \\
H^Q_{\mathfrak{s}} &\simeq \frac{\mathscr{Q}^2}{4(1-\mathscr{Q}^2)}\, G_{22}\, \mathfrak{s}^2 + O(\mathfrak{s}^4), \\
H^Q_{\mathfrak{q}} &\simeq \frac{1}{\mathscr{Q}^2} G_{22}\, \mathfrak{s}^4 + O(\mathfrak{s}^6)\,,
\end{aligned}
\tag{18}
$$

where $\mathscr{Q}^2 = 4\mathfrak{q}(1-\mathfrak{q}) < 1$ and we note that $G^2_{22} = \mathrm{Var}(P^2) = \langle\Psi|P^4|\Psi\rangle - \langle\Psi|P^2|\Psi\rangle^2$. The superscript Q indicates that the quantities are evaluated from the quantum matrix Q.

Unlike for a single parameter, the collective bound in (8) is not always saturable: the reason is incompatibility of the measurements for different parameters [38]. The conditions for saturating the multiparameter quantum CRLB have been discussed in a number of papers [37, 39–41]. For our particular case, they are fulfilled whenever the PSF amplitude is real, $\Psi(x)^* = \Psi(x)$, which will be assumed from now on.

We shall focus on finding measurements attaining the quantum limit, thus offering significant advantages with respect to conventional direct intensity measurements. In the general case of unequally bright sources ($\mathfrak{q} \neq 1/2$), the lack of symmetry makes this issue challenging and one cannot expect to find closed-form expressions for the optimal positive operator valued measures (POVMs) for all the values of the source parameters. However, this becomes viable when separations get very small. As already discussed, this is the most interesting regime, where conventional imaging techniques fail.

We start by specifying a basis in the signal space. A suitable choice is the set $\{|\Psi_n\rangle\}$ defined in terms of the spatial derivatives of the amplitude PSF:

$$
\langle x - x_0|\Psi_n\rangle = \frac{\partial^n}{\partial x^n}\Psi(x - x_0), \quad n = 0, 1, 2, \ldots, \tag{19}
$$

where x_0 is an arbitrary displacement in the x-representation. We convert this set into an orthonormal basis $\{|\Phi_n\rangle\}$ by the standard Gram-Schmidt process. In this basis, all results can be expressed in a PSF-independent form. Moreover, signals well centered on the origin and with small separation, are represented by low-dimensional states; i.e., $\rho_{\boldsymbol{\theta}} \to |\Phi_0\rangle\langle\Phi_0|$ for $\mathfrak{s}_0 \to x_0$, and $\mathfrak{s} \to 0$.

To estimate three independent parameters, the required POVM must have at least four elements. We therefore consider the following class of measurements $\Pi_j = |\pi_j\rangle\langle\pi_j|$, ($j = 0, \ldots, 3$). Note carefully that $\Pi_3 = \mathbb{1} - \Pi_0 - \Pi_1 - \Pi_2$, so only three of these are independent. The subsequent analysis is carried out in a 4-dimensional computational basis $\{|\Phi_0\rangle, \ldots, |\Phi_3\rangle\}$, wherein we expand $|\pi_j\rangle$ as

$$
|\pi_j\rangle = \sum_{k=0}^{3} C_{jk}|\Phi_k\rangle\,. \tag{20}
$$

In addition, we set $C_{00} = C_{10} = 0$ and $C_{20} \neq 0, C_{21} \neq 0$. Removing the C_{00} and C_{10} components makes the corresponding rank-one projectors orthogonal to the signal PSF, which is the crucial factor boosting the performance of the measurement. By changing the displacement x_0, the basis and the measurement itself is displaced.

Next, we expand the signal components up to the fourth order in the small parameters

$$|\Psi_\pm\rangle \simeq \left(G_{00}+\frac{a_\pm^2}{2}G_{02}+\frac{a_\pm^4}{24}G_{04}\right)|\Phi_0\rangle + \left(a_\pm G_{11}+\frac{a_\pm^3}{6}G_{13}\right)|\Phi_1\rangle + \left(\frac{a_\pm^2}{2}G_{22}+\frac{a_\pm^4}{24}G_{24}\right)|\Phi_2\rangle + \frac{a_\pm^3}{6}G_{33}|\Phi_3\rangle\,, \tag{21}$$

where $a_\pm = \mathfrak{s}_0 \pm \mathfrak{s} - x_0$ and $G_{nm} = \langle\Phi_n|\Psi_m\rangle$. Notice that for real valued amplitude PSFs, all Gs carrying both odd and even subscripts are zero. We also have $G_{nm} = 0$ for all $n > m$, by construction of the basis set.

We are set to evaluate the probabilities $p_j = \mathfrak{q}\langle\Psi_+|\Pi_j|\Psi_+\rangle + (1-\mathfrak{q})\langle\Psi_-|\Pi_j|\Psi_-\rangle$, and the corresponding classical Fisher information matrix per detection event:

$$F_{\alpha\beta} = \sum_{j=0}^{3}\frac{(\partial_\alpha p_j)(\partial_\beta p_j)}{p_j}\,. \tag{22}$$

The maximum of the classical Fisher information F is its quantum version Q, as Q is optimized over all POVMs. The corresponding precisions are thus related by $H_\alpha^Q \geq H_\alpha$.

Our initial strategy is to align the center of the measurement (20) with the signal centroid by letting $x_0 = \mathfrak{s}_0$. The calculation of the precisions turns out to be a very lengthy task, yet the final result is surprisingly simple

$$H_\alpha = \lambda H_\alpha^Q\,. \tag{23}$$

Therefore, H_α differs from the quantum limit precision by a factor

$$\lambda = \mathscr{Q}^2\mathscr{A}\,, \qquad \mathscr{A} = \frac{(C_{01}C_{12}-C_{02}C_{11})^2}{C_{01}^2+C_{11}^2} < 1\,. \tag{24}$$

The coefficient λ consists of the product of two factors: one depending solely on the intensities, the other depending on the measurement. For obvious reasons, the latter one will be called the quality factor of the measurement.

Two remarks are in order here. First, the performance of the measurement (20), when aligned with the centroid, scales with the same power of $\mathfrak{s}$ as the quantum limit does. The quantum limit is attained, but for a separation independent factor. This is true for all real-valued PSFs, no matter how we set the remaining free parameters of the measurement. Second, by optimizing those free parameters, the separation-independent factor λ can be made arbitrarily close to $\lambda_{\max} = \mathscr{Q}^2$. Hence, for balanced signals ($\mathfrak{q} = 1/2$), $\lambda_{\max} \to 1$ and the measurement (20) becomes optimal. Conversely, for unbalanced signals, the measurement is suboptimal and its performance worsens with $\mathfrak{q}$, approaching the limit $\lambda \to 0$ when $\mathfrak{q} \to 0$ and $\mathfrak{q} \to 1$.

Next, we show that quantum limits can be saturated for any $\mathfrak{q}$ by optimizing the displacement x_0. The key point is that in the limit $\mathfrak{s} \ll 1$, the precisions $H_\alpha(x_0)$, when considered as a function of the measurement displacement x_0, take a Lorentzian shape, as can be appreciated in Fig. 4 for the particular case of $H_\mathfrak{s}(x_0)$. On decreasing the signal separation, the Lorentzian narrows down, with its center approaching the signal centroid. We therefore adopt the model

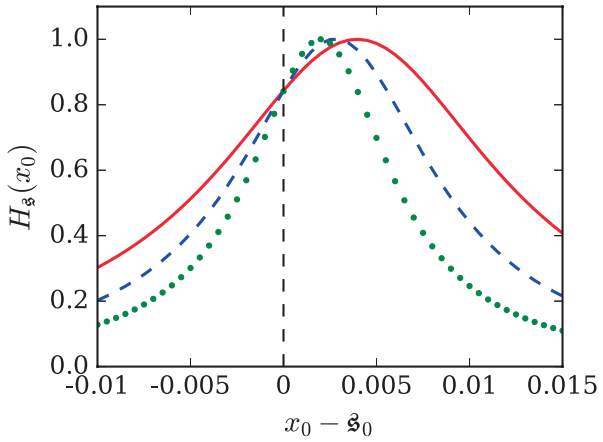

FIG. 4. The precision $H_\mathfrak{s}$ of the separation for point objects with relative intensities $\mathfrak{q} = 0.3$ and $\mathfrak{s} = 0.02$ (red solid line), $\mathfrak{s} = 0.014$ (blue broken line), and $\mathfrak{s} = 0.01$ (green dots) as a function of misalignment $x_0 - \mathfrak{s}_o$ between the measurement displacement and the centroid. The maxima of the Lorentzians are normalized to unity to make the changes in widths and centers apparent.

$$H_\mathfrak{s}(x_0) = \frac{\ell_1\mathfrak{s}^2}{1+\dfrac{\ell_2(x_0-\mathfrak{s}_0+\ell_3\mathfrak{s})^2}{\mathfrak{s}^2}}\,. \tag{25}$$

The parameters can be identified by expanding $H_\mathfrak{s}$ in $\mathfrak{s}$ and $x_0 - \mathfrak{s}_0$: $\ell_1\mathfrak{s}^2 = \mathscr{A}H_\mathfrak{s}^Q$, $\ell_2 = 1[\mathfrak{q}(1-\mathfrak{q})]$ and $\ell_3 = (1-2\mathfrak{q})/2$. This uncovers the optimal displacement and precisions

$$x_0^{\rm opt} = \arg\max_{x_0} H_\mathfrak{s}(x_0) = \mathfrak{s}_o - \tfrac{1}{2}\mathfrak{s}(1-2\mathfrak{q})\,, \qquad H_\alpha(x_0^{\rm opt}) = \mathscr{A}H_\alpha^Q\,. \tag{26}$$

This is the central result of this paper. The optimal choice of displacement is the same for all precisions and it is precisely at the center of mass of the intensity pattern $x_0^{\rm opt} = (1-\mathfrak{q})(\mathfrak{s}_0 - \mathfrak{s}/2) + \mathfrak{q}(\mathfrak{s}_0+\mathfrak{s}/2)$. This implies that the weighted centroid, rather than the geometrical centroid, plays the central role in aligning the measurement. By optimizing the measurement displacement x_0, the intensity dependent $\mathscr{Q}^2$ term is removed from (23) and (24) and the quantum CRLBs are saturated for all the signal parameters simply by letting $\mathscr{A} \to 1$. As this can be done in infinitely many ways, we conclude there are infinitely many measurements attaining the quantum limit

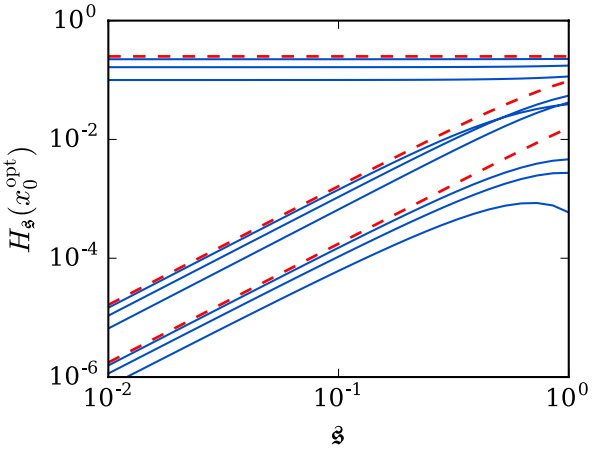

FIG. 5. The precision $H_{\mathfrak{s}}(x_0)$ for optimally displaced measurement (27) (blue lines) as compared to the quantum limit (18) (red broken line). The lines are grouped by the intensity difference: $\mathfrak{q}=0.5$ (top), $\mathfrak{q}=0.3$ (middle), and $\mathfrak{q}=0.1$ (bottom). Within each group (bottom to top) $\sin\theta=0.5$, $\sin\theta=0.7$, and $\sin\theta=0.9$, respectively. Notice the fast convergence towards the quantum limit over a wide range of separations. Gaussian PSF of a unit width $\sigma=1$ is assumed.

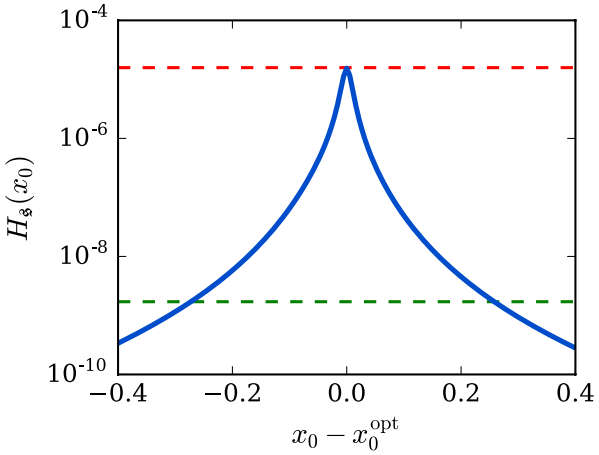

FIG. 6. The precision $H_{\mathfrak{s}}$ for a misaligned measurement (27), with $\sin\theta=0.99$, (blue solid line) compared to the corresponding quantum (top red) and direct imaging (bottom green) limits. Observe the log vertical scale. Gaussian PSF of a unit width $\sigma=1$ is assumed; and the sources satisfy $\mathfrak{s}=0.03$ and $\mathfrak{q}=0.1$.

in multiparameter superresolution imaging: they can be constructed along our recipe for any real-valued amplitude PSF.

To illustrate our result with a concrete example, we take

$$|\pi_0\rangle=\begin{pmatrix}0\\ \frac{1}{\sqrt{2}}\\ \frac{1}{\sqrt{2}}\\ 0\end{pmatrix},\quad |\pi_1\rangle=\begin{pmatrix}0\\ \frac{\sin\theta}{\sqrt{2}}\\ -\frac{\sin\theta}{\sqrt{2}}\\ \cos\theta\end{pmatrix},\quad |\pi_2\rangle=\begin{pmatrix}\frac{1}{\sqrt{2}}\\ \frac{\cos\theta}{2}\\ -\frac{\cos\theta}{2}\\ -\frac{\sin\theta}{\sqrt{2}}\end{pmatrix} \tag{27}$$

in the $|\Phi_k\rangle$-representation, to build a family of POVMs according to the recipe (20). With the exception of $\cos\theta=0$ this measurement satisfies all the requirements, and the quality factor becomes $\mathscr{A}=2\sin^2\theta/(1+\sin^2\theta)$. This goes to unity if $\sin\theta\to 1$, so that In the measurement (27) attains the quantum limit asymptotically for any real-valued PSF.

The theory thus far is largely independent of the actual form of the PSF. To be more specific we adopt a Gaussian PSF, with unit width $\sigma=1$, which will serve from now on as our basis unit length. The associated orthonormal basis is then a set of displaced Hermite-Gauss modes

$$\Phi_n(x)=\frac{1}{(2\pi)^{\frac{1}{4}}2^{\frac{n}{2}}\sqrt{n!}}H_n\left((x-x_0^{\rm opt})/\sqrt{2}\right)\exp[-\tfrac{1}{4}(x-x_0)^2], \tag{28}$$

so that $G_{22}=1/8$.

Figure 5 shows the resulting precision $H_{\mathfrak{s}}$ as a function of $\mathfrak{s}$ on a log-log scale for different intensities $\mathfrak{q}$ and quality factors $\mathscr{A}$. The data is obtained by direct numerical evaluation of the Fisher information (22) using a computational basis $\{\Phi_n\}$ of dimension 30 and no further approximation. In this case, the measurement (20) is not a Von Neumann projection, but a general POVM. As $\mathscr{A}\to 1$, the precisions quickly converge towards the quantum limit and the measurement (27) becomes optimal. We emphasize that the projections found for the simplified case of balanced sources [24] (projecting on a complete set such as, e.g., Hermite-Gauss modes) yields a singular Fisher matrix when extended to the multiparameter scenario and ultimately fails.

The performance will be compromised by any misalignment with respect to $x_0^{\rm opt}$. This effect is examined in Fig. 6, where the quantum limit and the direct intensity imaging are compared with a misaligned measurement (27) of quality $\mathscr{A}\simeq 0.99$. Being about two orders of magnitude below the Rayleigh limit, such imperfections cause a loss of precision. Even then, the advantage with respect to direct imaging persists over a wide range of displacements x_0, demonstrating the robustness of our detection scheme.

From a theoretical viewpoint, one may still find the new superresolution technique discussed here unsatisfactory, inasmuch as achieving the quantum limits requires knowing the true values of the measured parameters. In particular, the measurement must be optimally displaced to reach the quantum limits and this displacement, through (26), depends on all the unknown signal parameters. Consequently different displacements should be used for different signals.

Can one hope to saturate the quantum limits for all signals with a fixed measurement? Unfortunately, the answer is no.

Let us consider the estimation of a signal with strongly overlapping components $\mathfrak{s} \ll 1$ of highly unequal intensities $\mathfrak{q} \to 0$ (the same analysis can be carried out for $\mathfrak{q} \to 1$), so that the weak component is outshined. To gain significant information about the weak component, the bright one must be almost completely suppressed in one of the measurement outputs. This is ensured by projecting the signal on a state that is nearly orthogonal to the bright component. That crucial projection, though, depends on both the signal centroid and separation.

Our optimal measurement also behaves in this way. Let us look at the value of $x_0^{\rm opt}$ in the limit $\mathfrak{q} \to 0$; i.e., when $|\Psi_-\rangle$ is the bright component. In this case, $x_0^{\rm opt} \to \mathfrak{s}_0 - \mathfrak{s}$ coincides with the center of the bright component. But, this means that $|\Phi_0\rangle = |\Psi_-\rangle$ and the two outputs described by $|\pi_0\rangle$ and $|\pi_1\rangle$ project on subspaces orthogonal to the bright component, as anticipated.

Nonetheless, having a state-dependent measurement is not a major problem from the application point of view, where adaptive strategies can be used to approach the quantum limit in realistic scenarios. This technical point will be addressed in future work.

VII. CONCLUSIONS

In summary, we have presented a comprehensive analysis of the ultimate precision bounds for estimating the centroid, the separation, and the relative intensities of two point-like incoherent sources. For equally bright sources, the quantum Fisher information remains constant, which translates into the fact that the Rayleigh limit is not essential and can be lifted. On the other hand, for unequally bright sources, the information about very small separations always drops to near zero and the Rayleigh curse is unavoidable. Nonetheless, significant improvements can still be expected with optimal detection schemes. Particularly, for small separation the Quantum Fisher Bound can be saturated for the measurement corresponding to few projections onto a suitable complete set of modes. The optimal modes can be generated from the derivatives of the system PSF, however more work is needed for experimental realization of such a scheme.

[1] Lord Rayleigh, "Investigations in optics, with special reference to the spectroscope," Phil. Mag. **8**, 261–274 (1879).

[2] J. W. Goodman, *Introduction to Fourier Optics* (Roberts and Company, Englewood, 2004).

[3] A. J. den Dekker and A. van den Bos, "Resolution: a survey," J. Opt. Soc. Am. A **14**, 547–557 (1997).

[4] E. Betzig, G. H. Patterson, R. Sougrat, O. W. Lindwasser, S. Olenych, J. S. Bonifacino, M. W. Davidson, J. Lippincott-Schwartz, and H. F. Hess, "Imaging intracellular fluorescent proteins at nanometer resolution," Science **313**, 1642 (2006).

[5] S. T. Hess, T. P. K. Girirajan, and M. D. Mason, "Ultra-high resolution imaging by fluorescence photoactivation localization microscopy," Biophys. J. **91**, 4258–4272 (2006).

[6] S. W. Hell, "Far-field optical nanoscopy," Science **316**, 1153–1158 (2007).

[7] M. I. Kolobov, "Quantum Imaging," (Springer, Berlin, 2007) Chap. Quantum Limits of Optical Super-Resolution, pp. 113–138.

[8] Focus issue: Super-resolution Imaging, Nat. Photonics **3**, 361–420 (2009).

[9] S. W. W Hell, "Microscopy and its focal switch," Nat. Meth. **6**, 24–32 (2009).

[10] G. Patterson, M. Davidson, S. Manley, and J. Lippincott-Schwartz, "Superresolution imaging using single-molecule localization," Annu. Rev. Phys. Chem. **61**, 345–367 (2010).

[11] P. R. Hemmer and T. Zapata, "The universal scaling laws that determine the achievable resolution in different schemes for super-resolution imaging," J. Opt. **14**, 083002 (2012).

[12] C. Cremer and R. B. Masters, "Resolution enhancement techniques in microscopy," Eur. Phys. J. H **38**, 281–344 (2013).

[13] E. Abbe, "Ueber einen neuen Beleuchtungsapparat am Mikroskop," Arch. Mikrosk. Anat. **9**, 469–480 (1873).

[14] M. Tsang, R. Nair, and X.-M. Lu, "Quantum theory of superresolution for two incoherent optical point sources," Phys. Rev. X **6**, 031033 (2016).

[15] R. Nair and M. Tsang, "Far-field superresolution of thermal electromagnetic sources at the quantum limit," Phys. Rev. Lett. **117**, 190801 (2016).

[16] S. Z. Ang, R. Nair, and M. Tsang, "Quantum limit for two-dimensional resolution of two incoherent optical point sources," Phys. Rev. A **95**, 063847 (2016).

[17] M. Tsang, "Subdiffraction incoherent optical imaging via spatial-mode demultiplexing," New J. Phys. **19**, 023054 (2017).

[18] M. Paur, B. Stoklasa, Z. Hradil, L. L. Sanchez-Soto, and J. Rehacek, "Achieving the ultimate optical resolution," Optica **3**, 1144–1147 (2016).

[19] F. Yang, A. Taschilina, E. S. Moiseev, C. Simon, and A. I. Lvovsky, "Far-field linear optical superresolution via heterodyne detection in a higher-order local oscillator mode," Optica **3**, 1148–1152 (2016).

[20] W. K. Tham, H. Ferretti, and A. M. Steinberg, "Beating Rayleigh's curse by imaging using phase information," Phys. Rev. Lett. **118**, 070801 (2016).

[21] F. Yang, R. Nair, M. Tsang, C. Simon, and A. I. Lvovsky, "Fisher information for far-field linear optical superresolution via homodyne or heterodyne detection in a higher-

order local oscillator mode," arXiv.org:1706.08633 (2017), https://arxiv.org/pdf/1706.08633.pdf.
[22] C. Lupo and S. Pirandola, "Ultimate precision bound of quantum and subwavelength imaging," Phys. Rev. Lett. **117**, 190802 (2016).
[23] H. Krovi, S. Guha, and J. H. Shapiro, "Attaining the quantum limit of passive imaging," arXiv:16009.00684 (2016).
[24] J. Rehacek, M. Paúr, B. Stoklasa, Z. Hradil, and L. L. Sánchez-Soto, "Optimal measurements for resolution beyond the Rayleigh limit," Opt. Lett. **42**, 231–234 (2017).
[25] R. Kerviche, S. Guha, and A. Ashok, "Fundamental limit of resolving two point sources limited by an arbitrary point spread function," in *2017 IEEE International Symposium on Information Theory (ISIT)* (2017) pp. 441–445.
[26] Q. Zhuang, Z. Zhang, and J. H. Shapiro, "Quantum illumination for enhanced detection of Rayleigh-fading targets," Phys. Rev. A **96**, 020302 (2017).
[27] M. E. Pearce, E. T. Campbell, and P. Kok, "Optimal quantum metrology of distant black bodies," Quantum **1**, 21 (2017).
[28] A. Chrostowski, R. Demowicz-Dobrzański, M. Jarzyna, and K. Banaszek, "On superresolution imaging as a multiparameter estimation problemi," Int. J. Quantum Inf. **15** (2017).
[29] M. Tsang, "Quantum limits to optical point-source localization," Optica **2**, 646–653 (2015).
[30] R. Nair and M. Tsang, "Interferometric superlocalization of two incoherent optical point sources," Opt. Express **24**, 3684–3701 (2016).
[31] T. Z. Sheng, K. Durak, and A. Ling, "Fault-tolerant and finite-error localization for point emitters within the diffraction limit," Opt. Express **24**, 22004–22012 (2016).
[32] L. Mandel and E. Wolf, *Optical Coherence and Quantum Optics* (Cambridge University Press, Cambridge, 1995).
[33] D. Petz and C. Ghinea, "Introduction to Quantum Fisher Information," in *Quantum Probability and Related Topics*, Vol. Volume 27 (World Scientific, 2011) pp. 261–281.
[34] C. W. Helstrom, "Minimum mean-squared error of estimates in quantum statistics," Phys. Lett. A **25**, 101–102 (1967).
[35] M. G. A. Paris, "Quantum estimation for quantum technology," Int. J. Quantum Inform. **7**, 125–137 (2009).
[36] S. L. Braunstein and C. M. Caves, "Statistical distance and the geometry of quantum states," Phys. Rev. Lett. **72**, 3439–3443 (1994).
[37] M. Szczykulska, T. Baumgratz, and A. Datta, "Multi-parameter quantum metrology," Adv. Phys. **1**, 621–639 (2016).
[38] A. S. Holevo, *Probabilistic and Statistical Aspects of Quantum Theory*, 2nd ed. (North Holland, Amsterdam, 2003).
[39] K. Matsumoto, "A new approach to the Cramér-Rao-type bound of the pure-state model," J. Phys. A: Math. Gen. **35**, 3111 (2002).
[40] P. J. D. Crowley, A. Datta, M. Barbieri, and I. A. Walmsley, "Tradeoff in simultaneous quantum-limited phase and loss estimation in interferometry," Phys. Rev. A **89**, 023845 (2014).
[41] S. Ragy, M. Jarzyna, and R. Demkowicz-Dobrzański, "Compatibility in multiparameter quantum metrology," Phys. Rev. A **94**, 052108 (2016).
[42] J. M. Bernardo and A. F. M. Smith, *Bayesian Theory* (Wiley, Sussex, 2000).
[43] http://www.usno.navy.mil/usno/astrometry/optical-ir-prod/wds/dm3 .
[44] T. Barclay, D. Huber, J. F. Rowe, J. J. Fortney, C. V. Morley, E. V. Quintana, D. C. Fabrycky, G. Barentsen, S. Bloemen, J. L. Christiansen, B.-O. Demory, B. J. Fulton, J. M. Jenkins, F. Mullally, D. Ragozzine, S. E. Seader, A. Shporer, P. Tenenbaum, and S. E. Thompson, "Photometrically derived masses and radii of the planet and star in the tres-2 system," Astrophys. J. **761**, 53 (2012).
[45] L. Pezzè, M. A. Ciampini, N. Spagnolo, P. C. Humphreys, A. Datta, I. A. Walmsley, M. Barbieri, F Sciarrino, and A. Smerzi, "Optimal measurements for simultaneous quantum estimation of multiple phases," Phys. Rev. Lett. **119**, 130504 (2017).
[46] R. Horst and P. M. Pardalos, eds., *Handbook of Global Optimization* (Springer, Berlin, 1995).
[47] http://julia.org .